Biogeochemistry of the Kuroshio Large Meander

Hakase Hayashida[1,2], Andrew E. Kiss[3,4], Toru Miyama[1], Yasumasa Miyazawa[1], and Sayaka Yasunaka[5]

[1]Application Laboratory, Japan Agency for Marine-Earth Science and Technology, Yokohama, Kanagawa, Japan

[2]Institute for Marine and Antarctic Studies, University of Tasmania, Hobart, TAS, Australia

[3]Research School of Earth Sciences, Australian National University, Canberra, ACT, Australia

[4]Australian Research Council Centre of Excellence for Climate Extremes, Australia

[5]Graduate School of Science, Tohoku University, Sendai, Japan

Corresponding author: Hakase Hayashida (hakaseh@jamstec.go.jp)

Key Points:

- The Kuroshio large meander (LM) expands the nutrient-rich surface water south of Japan further offshore during winter.
- During LM, phytoplankton spring blooms increase offshore due to nutrient enrichment and decrease nearshore due to nutrient reduction.
- In addition to thermal disturbance, the biogeochemical impacts of the large meander exert bottom-up control on higher trophic levels.

Abstract

The large meander of the Kuroshio western boundary current is well known to influence the local climate, fisheries, and aquaculture by greatly modulating regional heat transport, but its impacts on biogeochemical processes remain unclear. Using high-resolution numerical ocean modelling and long-term observational datasets, we show that the path of the Kuroshio determines the extent of the shallow nutricline region, where winter convective mixing replenishes nutrient availability for subsequent blooms of phytoplankton during spring. During the large meander phase, this mechanism triggers offshore phytoplankton blooms that are otherwise absent during the non-large meander phase. The large meander also modulates the spatial distributions of primary production, air-sea carbon flux, and export production. These biogeochemical impacts of the Kuroshio large meander exert bottom-up control on regional marine ecosystems that is disproportionate to the thermal effect, and therefore need to be assessed to understand the large meander's overall impacts on fisheries and aquaculture.

Plain Language Summary

The Kuroshio is one of the world's most powerful ocean currents that regulates the global distribution of heat, salt, and chemical elements by transporting a significant amount of seawater from one region to another. The Kuroshio generally travels along the southern coast of Japan, but from time to time, it deflects its pathway further south, often by more than 300 km. This deflection is known as the Kuroshio large meander, which has been discovered to have impacts on the weather, fisheries, and aquaculture in Japan. These impacts have been attributed to the large meander's ability to displace the heat distribution. However, the large meander's impact is beyond just heat, and so we need to understand what happens to other oceanic properties during the large meander, in order to understand its overall impact. In this study, we used a computer ocean model to simulate long large meander periods to characterize the impacts of the large meander on marine biogeochemistry. The results show that the large meander displaces the locations of high and low nutrient, which fuels phytoplankton to bloom in areas where they will not be able to otherwise. Understanding such changes is essential for better understanding the impacts on fish.

1 Introduction

The Kuroshio, which means *black current* in Japanese, is one of the strongest currents in the ocean that has significant impacts on the global climate system and local marine industries. Among the western boundary currents, the Kuroshio is unique in that its main path can be characterized by two stable states that it switches between on a timescale of a few years to a few decades (Kawabe, 1987). One of the these states takes the path that travels nearshore along the southern coast of Japan, which we refer to as the non-large meander. The other stable state, which is the main focus of this study, is the path that is deflected offshore south of the Tokai region, and is referred to as the large meander. As the Kuroshio is rapid and carries a huge

amount of water mass along with heat and materials in the ocean, the path of the Kuroshio is important for shipping, commercial fishing, and fish farming.

Since August 2017, the Kuroshio has been taking the large meander path. In April 2022, this large meander event has lasted for 4 years and 9 months, which has become the longest ever recorded large meander since a consistent observation by the Japan Meteorological Agency started in the 1960s (Qiu & Chen, 2021). The ongoing large meander has received much media attention in Japan, as it has been revealed to trigger extratropical cyclones with extreme rainfall (Hirata et al., 2019; Tochimoto & Iizuka, 2022), cause discomfort in summer over the greater Tokyo metropolitan area (Sugimoto et al., 2021), and modify the seasonal abundance and distribution of commercial fish (Chang et al., 2019; Zhu et al., 2021). All these reported impacts have been linked to the large meander's influence on physical conditions such as temperature, but obviously the large meander modulates other processes such as biogeochemistry. For example, nutrient and phytoplankton abundance can exert bottom-up control on the marine food web, which may have impacts on higher trophic levels such as commercial fish (e.g., Yoneda et al., 2022). However, such biogeochemical aspects of the larger meander have been explored only by a few studies (e.g., Lizarbe Barreto et al., 2021; Long et al., 2018), perhaps due to the lack of adequate samples to draw robust conclusions.

In this study, we characterize the biogeochemical impacts of the Kuroshio large meander by analyzing the multi-decadal output of a high-resolution global sea ice-ocean model simulation. Results reveal robust differences in the spatial distributions of nutrient, phytoplankton, primary production, ocean carbon uptake, and export production during the large meander phase compared to the non-large meander phase. Using available observations, we show that the simulated nutrient results are realistic, which shapes the rest of the biogeochemical quantities.

2 Methods

2.1 Kuroshio Large Meander Definition

The path of the Kuroshio is considered a large meander when it deflects far south of Japan for a prolonged period. Otherwise, the path is considered non-large meander. There are several indices to define the large meander, but their time series are generally consistent (Qiu & Chen, 2021). Here, the Kuroshio path is defined as a large meander when the southernmost axis of the Kuroshio is located south of 32°N in the 136-140°E segment. This definition is one of the two criteria for large meander determination used by the Japan Meteorological Agency (Sakajo et al., 2022). The other criterion is the sea level difference between Kushimoto and Uragami which is disregarded here because these two locations are much closer than the horizontal resolution of our model (Section 2.2). The Kuroshio axis is defined as the latitude at which the absolute meridional gradient of sea surface height is maximum, which corresponds to the approximate location of the fastest zonal geostrophic flow. Using this definition for the Kuroshio axis, we define a large meander event when the 13-month central moving average Kuroshio axis is

93 located south of 32°N for at least 12 consecutive months. Our definition matches well with the
94 past large meander events determined by the Japan Meteorological Agency (Figure A1).

95 To assess the model performance in simulating the Kuroshio path variability, we downloaded the
96 monthly Kuroshio axis time series produced by the Japan Meteorological Agency
97 (https://www.data.jma.go.jp/kaiyou/data/shindan/b_2/kuroshio_stream/kuro_slat.txt; last
98 accessed on November 15, 2022). The data provide the southernmost latitude of the Kuroshio in
99 the 136-140°E segment from 1961 to 2021 determined based on satellite and hydrographic
100 observations (Qiu & Chen, 2021; Sakajo et al., 2022). The data contain several missing values
101 during 1961-1968 and 1992-1999 (Figure A1).

102 **2.2 Model**

103 The global sea ice-ocean coupled numerical model used in this study is the 0.1° version of the
104 Australian Community Climate and Earth System Simulator - Ocean Model version 2 (ACCESS-
105 OM2-01), an updated version of the configuration described by Kiss et al. (2020). The physical
106 model is composed of the Modular Ocean Model (MOM) version 5.1 and the Los Alamos sea ice
107 model (CICE) version 5.1.2. The biogeochemical model is composed of the Whole Ocean Model
108 of Biogeochemistry and Trophic-dynamics (WOMBAT; Oke et al., 2013) and the
109 biogeochemistry of CICE (Jeffery et al., 2016). WOMBAT is a phosphorous-based four-
110 component (Nutrient-Phytoplankton-Zooplankton-Detritus; NPZD) model with carbonate
111 chemistry, dissolved oxygen, and bioavailable dissolved iron (Oke et al., 2013). Phosphate is the
112 only macronutrient tracer, and a fixed Redfield ratio of 1:16:106:−172 is assumed with
113 phosphorous, nitrogen, carbon, and oxygen. We use the same biogeochemical parameters as
114 Ziehn et al. (2020). Although the micronutrient iron can limit the phytoplankton growth, it is not
115 the limiting factor for the Kuroshio region (Hayashida et al., 2020), which is supported by
116 available observations (Moore et al., 2013). There is no supply of nutrient from river discharge,
117 but this effect may be negligible for the nutrient budget in the study region which is further away
118 from river mouths (Kuroda et al., 2018).

119 In this study, we analyzed the monthly mean output of ACCESS-OM2-01 which was integrated
120 for 244 years by prescribing the 61-year (1958-2018) Japanese Atmospheric Reanalysis dataset
121 (JRA55-do version 1.4.0; Tsujino et al., 2018) as the surface forcing repeatedly for four times.
122 This cyclic procedure follows the protocol of the Ocean Model Intercomparison Project (OMIP;
123 Griffies et al., 2016; Tsujino et al., 2020). The ocean model was initialized from rest with zero
124 sea level anomaly, and the initial temperature and salinity fields were set to the World Ocean
125 Atlas 2013 version 2. The first three cycles were integrated using the physics-only version of
126 ACCESS-OM2-01. The biogeochemistry model was incorporated at the beginning of the fourth
127 cycle and integrated for 61 years (Years 184-244). The biogeochemical fields were initialized at
128 the start of the fourth cycle to the Global Ocean Data Analysis Project version 2 (GLODAPv2;
129 Lauvset et al., 2016) for dissolved nitrate (via the Redfield ratio), the multi-model median values
130 of the Iron Model Intercomparison Project for dissolved iron (Tagliabue et al., 2016), and an

arbitrary small value globally (0.625 nM phosphorous) for phytoplankton, zooplankton, detritus, and calcium carbonate. To expedite the spin-up of dissolved inorganic carbon and total alkalinity, these fields were initialized to their end states of the fifth cycle of the OMIP simulation using the lower-resolution (1°) ACCESS-OM2 (omip2; Mackallah et al., 2022; Orr et al., 2017). Unlike the other biogeochemical fields, dissolved oxygen was initialized to GLODAPv2 21 years later (model year 205; forcing year 1979) due to a bug in the initialization routine. Dissolved oxygen has no effect on other biogeochemical tracers, and the biogeochemical tracers have no effect on the physical state.

2.3 Observation-based Surface Phosphate Gridded Dataset

To evaluate the model performance in simulating the nutrient concentration distributions in the Kuroshio region, we generated monthly composite maps of observation-based surface phosphate concentrations for the large meander and non-large meander phases. This dataset is an updated version of the 1° gridded product over the North Pacific based on optimal interpolation of in situ measurements from 1961 to 2021 (Yasunaka et al., 2021). The updates incorporate recent measurements archived in the World Ocean Database 2018 (Boyer et al., 2018) and the Global Ocean Data Analysis Project v2.2022 (Lauvset et al., 2022), which allows us to increase the number of samples for the large meander composites. The decorrelation radius for the optimal interpolation was set to 7° both in the zonal and meridional directions and 1 month in the temporal direction. The signal-to-noise ratio was set to 1.7; the interpolated data whose interpolation square error ratios are less than 0.9 were used in this study.

2.4 Long-term Phosphate Monitoring along 137°E

To evaluate the simulated difference in the nutrient distribution between the large meander and non-large meander states, we downloaded the hydrographic transect dataset along 137°E provided by the Japan Meteorological Agency (https://www.data.jma.go.jp/gmd/kaiyou/db/mar_env/results/OI/137E_OI_e.html; last accessed on November 15, 2022). The dataset provides a collection of more than 50 years of ship-based oceanographic observations since 1967 (Oka et al., 2018). In this study, we analyzed the dissolved phosphate concentrations collected by water sampling annually during winter (between late January and early February) from 1997 to 2022, covering 6 large meander years and 20 non-large meander years (Figure A2). The measured units of μmol kg^{-1} were converted to the units of the model output (μM) using the density of the water sample. We used the phosphate samples with a quality control flag of 2, which means *acceptable measurement* for water samples

following the definition of the World Ocean Circulation Experiment (WOCE; https://www.ewoce.org/; last accessed on November 15, 2022).

3 Results

3.1 Kuroshio Path Variability

During the 244 years of the model integration, the model simulated 13 large meander events which lasted for 1 to 15 years (Figure 1a). Even though the same 61-year interannual variability was prescribed as the atmospheric forcing repeatedly for four times, the Kuroshio path variability is different among the four cycles of this free-running (i.e., not data-assimilating) model. This finding demonstrates the importance of ocean dynamics in determining the Kuroshio path variability and that the variability is unpredictable from the atmospheric state alone, which is consistent with the findings of the previous studies (Qiu & Miao, 2000; Tsujino et al., 2013).

To evaluate the simulated Kuroshio path variability, the probability density distributions of the Kuroshio axis in the model and the observations are compared (Figure 1b-d). Both the model and the observations agree that the distributions are skewed to the left of the median. Median values are 32-33°N, indicating the dominance of the non-large meander states. The model has a bias in simulating the most frequent Kuroshio axis positioned at 32.6-32.8°N (Figure 1b), which is about 0.4° south of the most frequent observed axis (Figure 1c). In terms of the distributions south of 32°N, the model tends to simulate large meanders positioned at 30.4-30.6°N, as indicated by the secondary peak in the histogram (Figure 1b). Furthermore, the model very occasionally simulates large meanders that are positioned south of 29°N (Figure 1a,b). Both of

these simulated features are absent in the observations (Figure 1c). The modelled distribution is also much more clearly bimodal than the observed distribution.

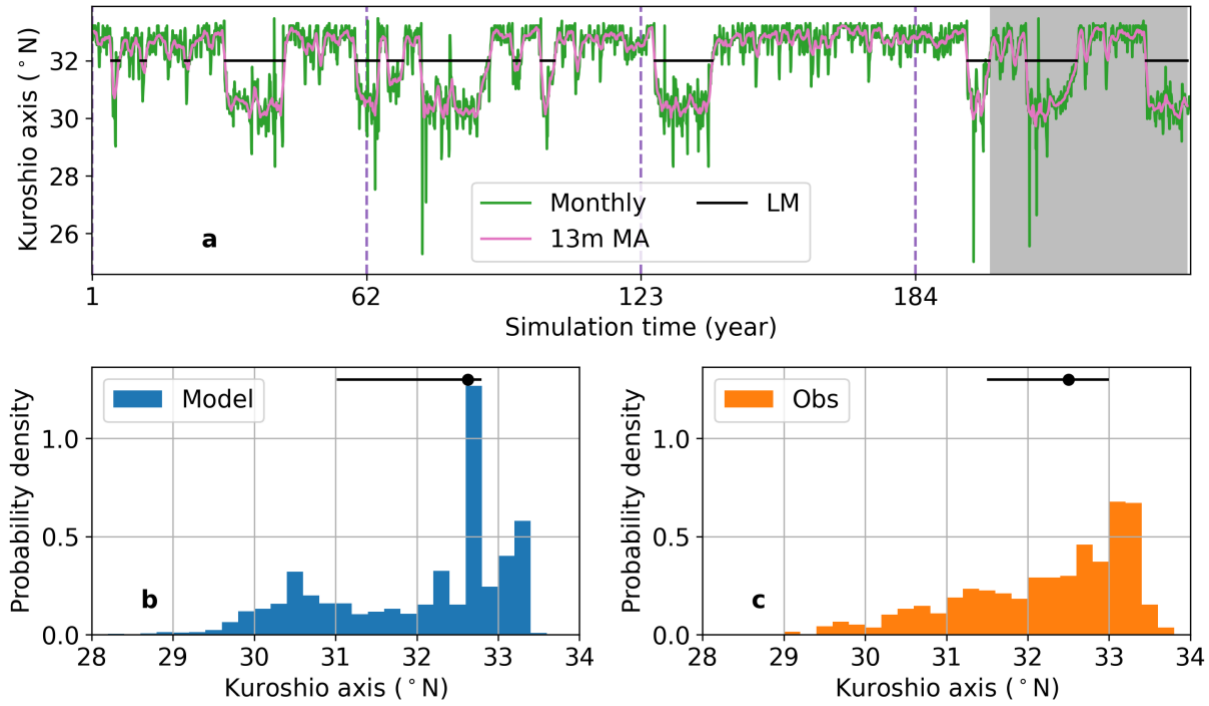

Figure 1. (a) Monthly time series of the Kuroshio axis latitude over the 244 years of the model integration. Green denotes monthly values with the 13-month central moving average indicated by pink. Horizontal black line segments along 32°N denote the large meander events. Vertical purple dashed lines indicate the first year of each cycle for the atmospheric forcing. Shading denotes the large meander and non-large meander events used for biogeochemical model composite analysis. Comparisons of the monthly Kuroshio axis probability density distributions with a latitudinal bin size of 0.2° (b) simulated by the model over 244 years with (c) those determined observationally over 1961-2021 by the Japan Meteorological Agency (JMA). In (b-c), dots show the median Kuroshio axis with horizontal lines denoting the interquartile range.

3.2 Nutrient and Phytoplankton

In the last 61 years of the model integration during which the biogeochemical model was incorporated, we consider the first 15 years or so as a spin-up phase based on the time series of modelled biogeochemical properties averaged over the Kuroshio region (Figure A3). We therefore characterized the biogeochemical structure of the large meander and non-large meander states based on the last 44 years of the model integration. During this period, the model simulated two large meander periods and two non-large meander periods, each of which lasted for between 8 and 15 years (Figure 1a). This resulted in a total of 246 large-meander and 282 non-large-meander monthly samples of the model output. From these rich samples, we

constructed large meander and non-large meander composites of modelled dissolved phosphate concentration and phytoplankton biomass distributions.

For phosphate, the difference between the large meander and non-large meander phases is most prominent during winter (February; Figure 2). The large meander is well known to generate a persistent cold-core eddy offshore north of the Kuroshio path at around 137°E (Sugimoto et al., 2020). As expected from the general characteristics of cold-core eddies (Chang et al., 2017), our results show that this cyclonic eddy is rich in phosphate (Figure 2a). The transect along 137°E shows that the subsurface phosphate is shoaled on the north side of the Kuroshio (Figure 2d). By comparing the depths of nutricline (the maximum absolute vertical gradient in nutrient concentrations) between the north and south of the Kuroshio, we estimate this shoaling effect to be about 400 m.

During non-large meander phases, the phosphate-rich surface water is limited to nearshore areas, and similar to the large meander phases, it is located north of the Kuroshio path (Figure 2b). The transect along 137°E illustrates that the shoaling of subsurface nutrient-rich water is narrower but stronger than the large meander cases, as depicted by the greater difference in the nutricline depth across the Kuroshio (about 500 m; Figure 2e). As a result, the surface phosphate concentration difference between the large meander and the non-large meander can be characterized by higher offshore concentrations and lower nearshore concentrations during the large meanders, and vice versa for the non-large meanders (Figure 2c). This difference is controlled by the changes in the extent and strength of the shoaling of the subsurface phosphate-rich water determined by the position and strength of the Kuroshio (Figure 2f). Enhanced shoaling during the non-large meander states may be related to topographic features (Miyama & Miyazawa, 2013).

The winter phosphate concentration difference between the large meander and non-large meander states preconditions the annual bloom of phytoplankton in these typically nutrient-limited regions during spring (May; Figure 3). Phytoplankton spring blooms respond positively to the offshore nutrient enrichment and negatively to the nearshore nutrient reduction triggered by large meanders (Figure 3c), which mirrors the spatial pattern of the winter surface phosphate concentration difference (Figure 2c). Phytoplankton biomass within 1-2° south of the Kuroshio is generally low.

The vertical extent of the offshore bloom during the large meander is about 20 m deeper than that of the nearshore bloom present in both the large meander and non-large meander states (Figure 3d,e). The nearshore bloom is slightly weaker during the large meander. Hence, the

primary difference is that the large meander expands the latitudinal extent of the spring bloom north of the Kuroshio by as much as 300 km along 137°E.

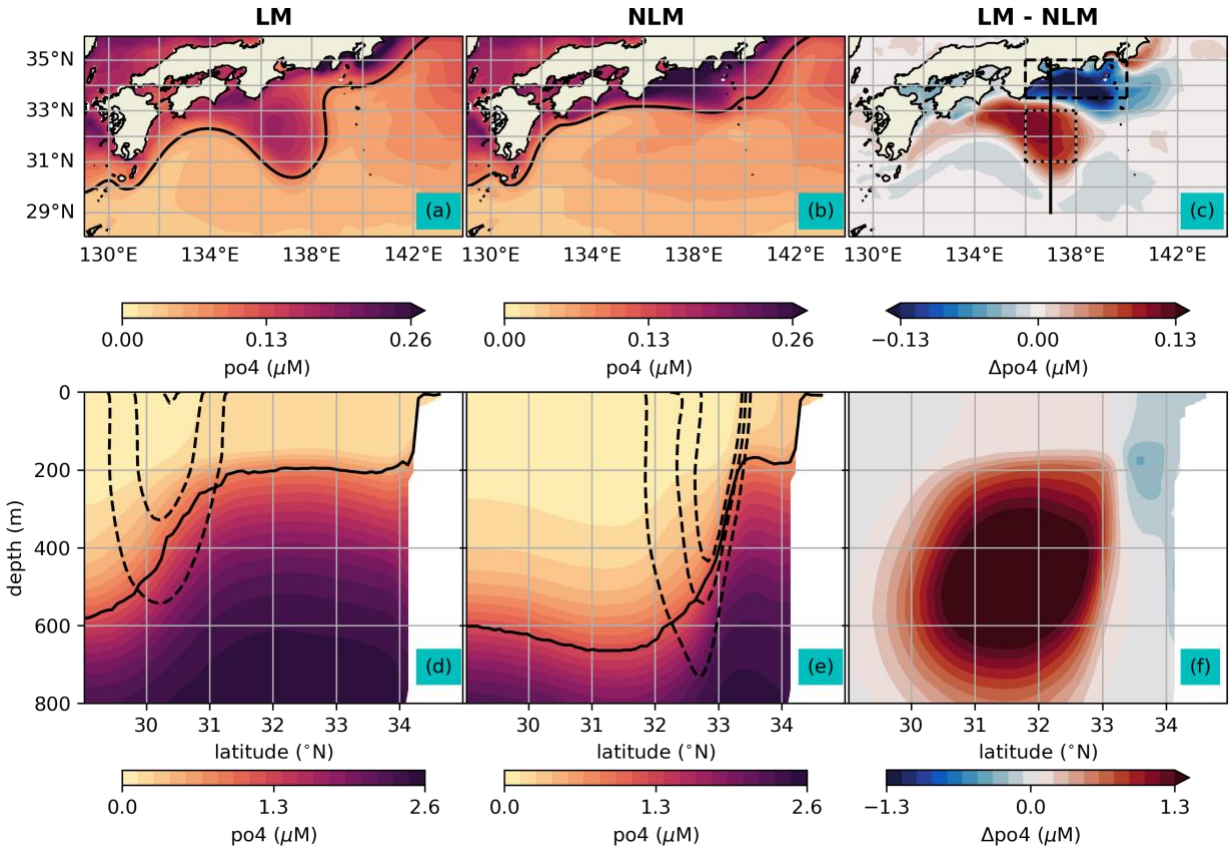

Figure 2. Comparisons of modelled February composite surface dissolved phosphate concentration south of Japan during (a) the large meander and (b) the non-large meander, and (c) their difference. (d-f) Cross-section comparisons in the upper 800 m along 137°E, denoted by black solid line in (c). Solid lines in (a) and (b) represent the path of the Kuroshio, defined by the sea level contour at which the latitudinal gradient is maximum along 137°E. Dashed and dotted boxes in (c) define respectively the nearshore and offshore regions used for time series analysis

in Figure 6. Solid and dashed lines in (d) and (e) represent the nutricline and the zonal velocity contours of 0.2, 0.4, and 0.6 m s^{-1}, respectively.

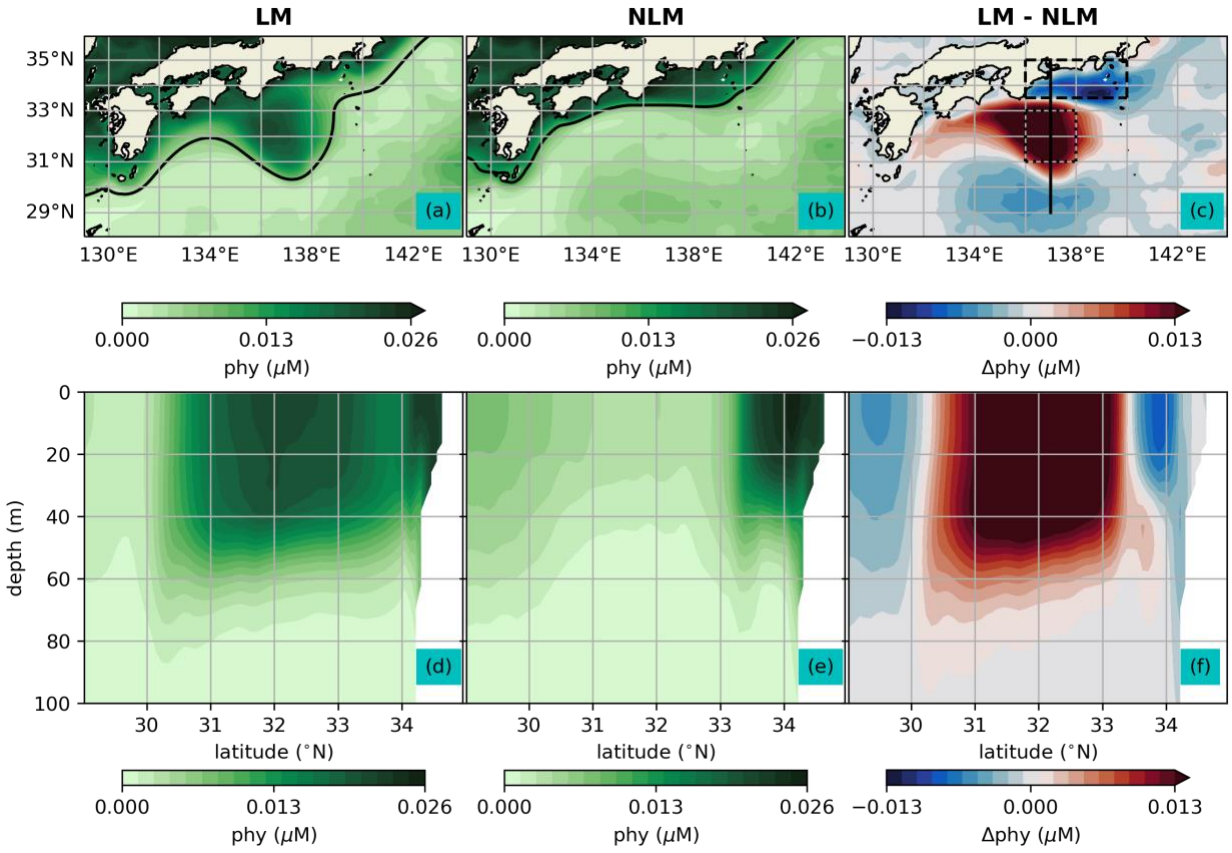

Figure 3. Comparisons of modelled May composite surface phytoplankton phosphorous biomass south of Japan during (a) the large meander and (b) the non-large meander, and (c) their difference. (d-f) Cross-section comparisons in the upper 100 m along 137°E, denoted by black solid line in (c). Solid lines in (a) and (b) represent the path of the Kuroshio, defined by the sea level contour at which the latitudinal gradient is maximum along 137°E. Dashed and dotted boxes in (c) define respectively the nearshore and offshore regions used for time series analysis in Figure 6.

3.2.1 Consistency with Observations

The observation-based surface dissolved phosphate concentration dataset illustrates both the offshore enrichment and the nearshore reduction of nutrients during the large meander winters as found in the model simulation (Figure 4c). However, the magnitude of the phosphate concentration difference is much smaller in the observation-based dataset than the model. The observed offshore phosphate enrichment is about 0.05 μM (Figure 4c), which is about half of the modelled increase (Figure 4f). The observed nearshore phosphate reduction is only about 0.02 μM (Figure 4c), whereas the modelled reduction is close to 0.1 μM (Figure 4f). The observation-based dataset generally shows much smaller difference across the entire domain, possibly due to

interpolation with smoothing to minimize the error from sparse in-situ data which can result in suppressing variability (Yasunaka et al., 2021).

To further evaluate the model performance, we used the vertical profiles of dissolved phosphate concentrations along 137°E observed annually during winter over the last 26 years (Figure 5). The vertical profiles are available at every 1° latitude (Figure A2), but our analysis focused on the profiles at 29°N, 32°N, and 34°N, which respectively correspond to regions of neutral, positive, and negative anomalies in the modelled winter phosphate concentrations during the large meander relative to the non-large meander (Figure 2c,f). In general, the model underestimates the phosphate concentration below the surface mixed layer.

The observed profiles show no clear distinction between the large meander and non-large meander states at 29°N, which is consistent with the model (Figure 5a). At 32°N, there is a robust difference throughout the depth between the two phases (Figure 5b); the observed concentrations at every vertical level were always higher during the large meander than those of the non-large meander. This robust distinction is also evident from the model simulation. Within the surface mixed layer, the observed concentration difference is about 0.1 μM. Below the surface mixed layer, the observed concentration difference increases with depth up to about 1.8 μM at 400 m, and then decreases (Figure 5b). A very similar concentration difference in terms of both the magnitude and the vertical variation is simulated by the model.

At 34°N, the observed profiles generally show 0.1-0.5 μM lower phosphate concentrations during the large meander than the non-large meander in the surface mixed layer (Figure 5c), with an exception of one large meander year (2018; Figure A2). Below the surface mixed layer, the difference is indistinguishable between the large meander and non-large meander phases. The

model also simulates about 0.1 μM lower phosphate concentrations during the large meanders on average, extending from the surface mixed layer to about 400 m.

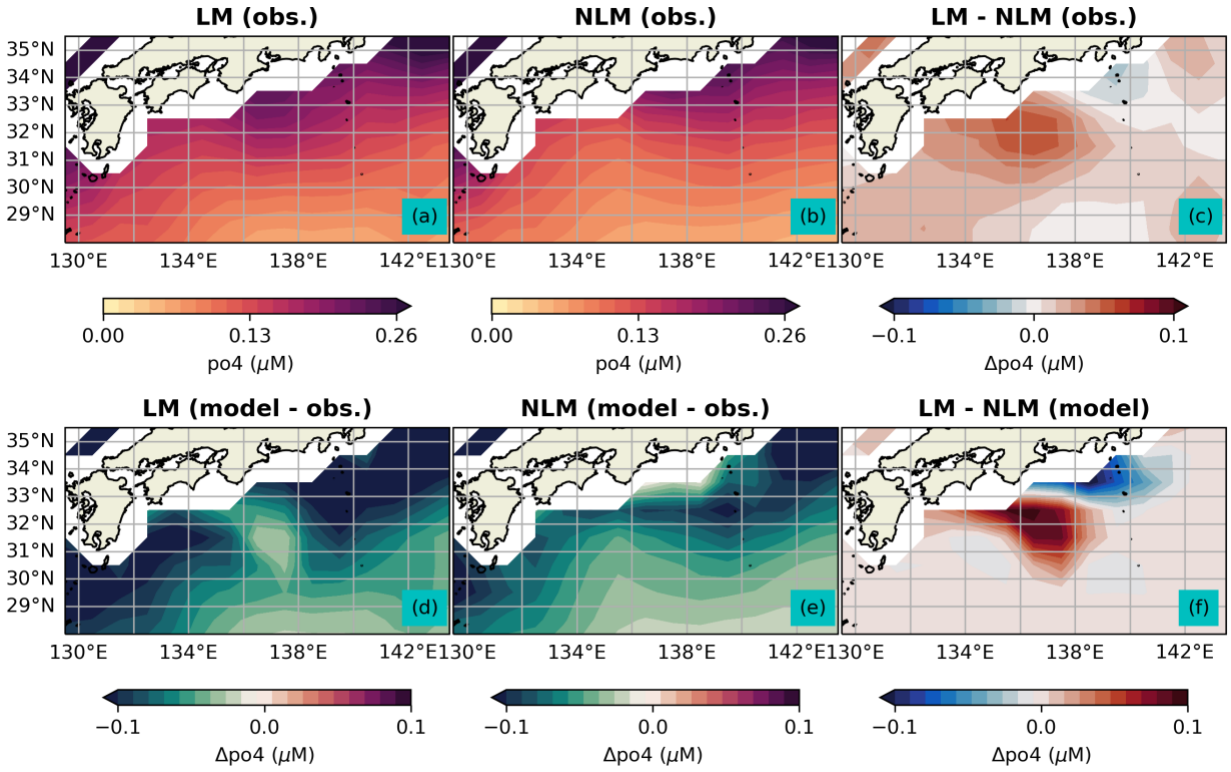

Figure 4. Comparison of observation-based January-February composite surface phosphate concentration south of Japan during (a) the large meander and (b) the non-large meander, and (c) their difference. Differences between the modelled and observation-based composites during (d) the large meander and (e) the non-large meander. (f) Difference between the large meander and

non-large meander composites of the model output. Here, the model output is interpolated to the grid of the observation-based dataset.

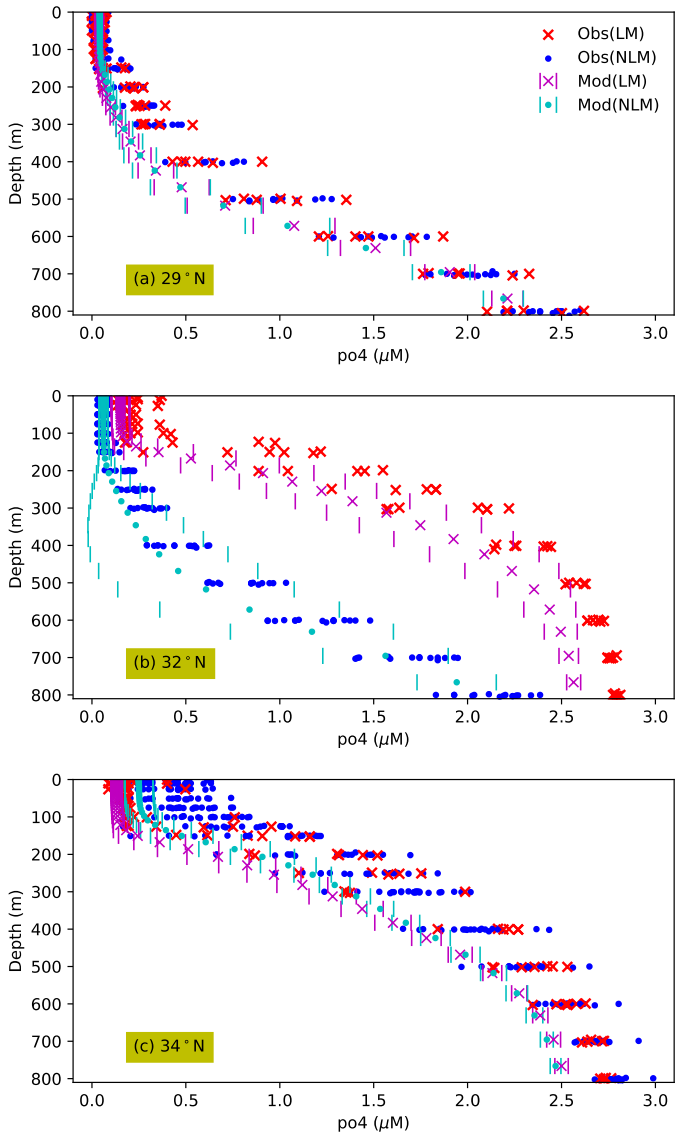

Figure 5. Comparisons of vertical dissolved phosphate concentration profiles in the upper 800 m between the large (LM; red) and non-large (NLM; blue) meander years at (a) 29°N, (b) 32°N, and (c) 34°N along 137°E collected between late-January and early-February annually since 1997. Magenta and cyan show the comparable profiles simulated by the model with errorbars denoting ±1 standard deviations from the January-February averages.

3.2.2 Seasonal Cycle

The biogeochemical impacts of the large meander have distinct seasonality as illustrated by the seasonal cycle comparison at the offshore and nearshore regions where the most prominent differences were identified (Figure 6). Both at the offshore and nearshore regions, the nutrient

concentration differences are robust from December to March, meaning that the concentrations between the large meander and non-large meander cases do not overlap even within one standard deviation ranges around their means (Figure 6a,b). Nutrient concentration differences decrease from April and are negligible from June to October, during which the concentrations are close to zero. In contrast, the nutricline depth does not vary seasonally at either location, and the differences between the large meanders and the non-large meanders are clear (Figure 6c,d). The lack of seasonality in the nutricline depth suggests that the surface nutrient concentration differences emerge only during winter because they are driven by winter convective mixing, and not processes that do not have specific seasonality such as eddy suction (Chang et al., 2017). The large meander enhances the winter nutrient replenishment in the offshore region by shoaling the nutricline depth (Figure 6c), thereby yielding higher surface nutrient concentrations compared to the non-large meander phases (Figure 6a). In contrast, the nearshore nutrient replenishment is stronger during the non-large meander phases when the shoaling effect of the Kuroshio is stronger (Figure 6d), resulting in higher surface nutrient concentrations than the large-meander case (Figure 6b). The mixed layer depth is always shallower in the offshore region during the large meander winters (January-March; Figure 6e), which rules out the possibility that the strength of the convective mixing drives the offshore nutrient enrichment. In other words, the shoaling effect of the nutricline overwhelms that of the mixed layer.

The seasonal cycles of modelled surface phytoplankton biomass reveal that the large meander changes not only the magnitude, but also the timing of the spring bloom in the offshore region (Figure 6g). The increased supply of phosphate during winter enables phytoplankton to form a bloom offshore that peaks in May. In the case of the non-large meander, the peak arrives a month later in June. In the nearshore region, the seasonality can be characterized by a spring bloom that peaks in May, which is common to both the large meander and non-large meander phases (Figure 6h). The only difference is that the biomass is consistently higher during the non-large meander phases, which is likely caused by the difference in the nutrient availability (Figure 6b). The higher biomass during large meanders in the offshore region and during non-large meanders in the nearshore region continues even in summer, which indicates the continuous nutrient input

from the subsurface thanks to the shallow nutricline. Surface phosphate concentrations remain low probably because nutrients are consumed as soon as they are supplied.

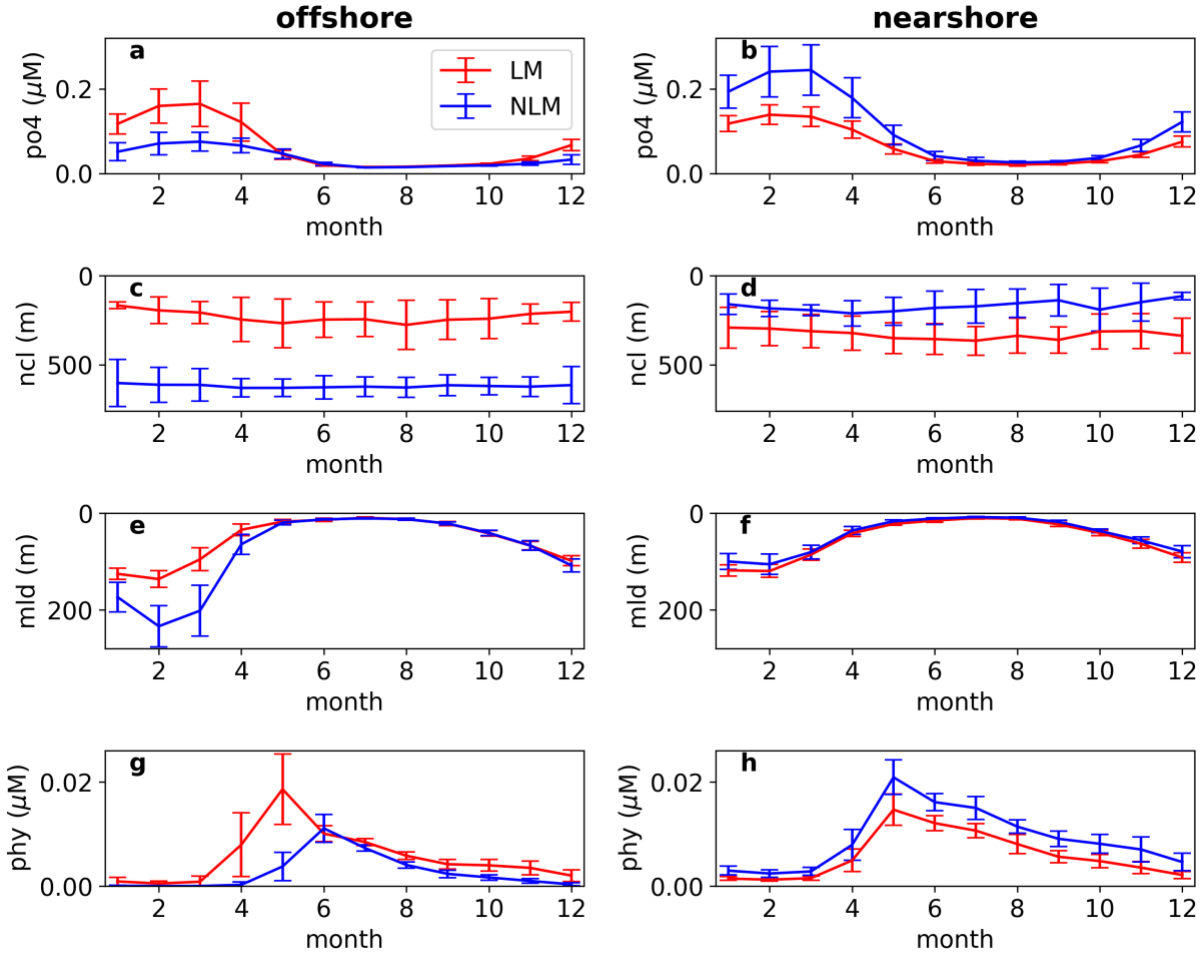

Figure 6. Comparisons of modelled monthly composite seasonal cycles of (a,b) surface dissolved phosphate concentration, (c,d) nutricline depth, (e,f) mixed layer depth, and (g,h) phytoplankton phosphorous biomass averaged over the (a,c) offshore and (b,d) nearshore regions defined in Figure 2 during the large (red) and non-large (blue) meander phases. Error bars represent the standard deviations of monthly area-averaged values incorporated into each phase.

3.2.3 Latitudinal Distributions and Correlations

The latitudinal position of the Kuroshio has strong influence on the latitudinal distributions of winter nutrient availability and spring phytoplankton biomass in the Kuroshio region (Figure 7a,b). There is a clear pattern that the north of the Kuroshio is always higher in phosphate concentration and phytoplankton biomass than its southern counterparts. However, there are a few exceptions that can be categorized into two groups. First, the phosphate concentration and the phytoplankton biomass 1° north of the Kuroshio are higher but they decrease further north until reaching near the coast in some cases (e.g., Year 239). This pattern emerges when the Kuroshio takes the S-shaped path (Kasai et al., 1993) along 137°N (Figure A4). In this case, it is

more appropriate to refer to the position of the phosphate-rich surface water (and hence the shallow nutricline area) as being left of the Kuroshio path, rather than the north of the Kuroshio. The other exception to the latitudinal distributions relative to the Kuroshio position is the presence of higher values further south of the Kuroshio that are especially evident from the phytoplankton biomass distribution (e.g., the first 4 years; Figure 7b). This pattern likely reflects local blooms south of the Kuroshio path, which would be located further south during the large meanders.

To elucidate the relationship between winter nutrient availability and spring phytoplankton bloom in the Kuroshio region, we calculated correlations between the two variables at each latitude along 137°N (Figure 7c). Correlation coefficients are above 0.6 throughout the latitudes between 30.7-33.3°N, indicating the strong relationship between winter nutrient availability and the subsequent bloom strength on a year-to-year basis. Correlations are weaker north of this latitudinal band probably because the phosphate concentration is generally high in the nearshore region, and so there must be other processes that drive the interannual variability of the spring bloom magnitude. Correlations are generally also weaker south of 30.7°N (except around 29.5°N).

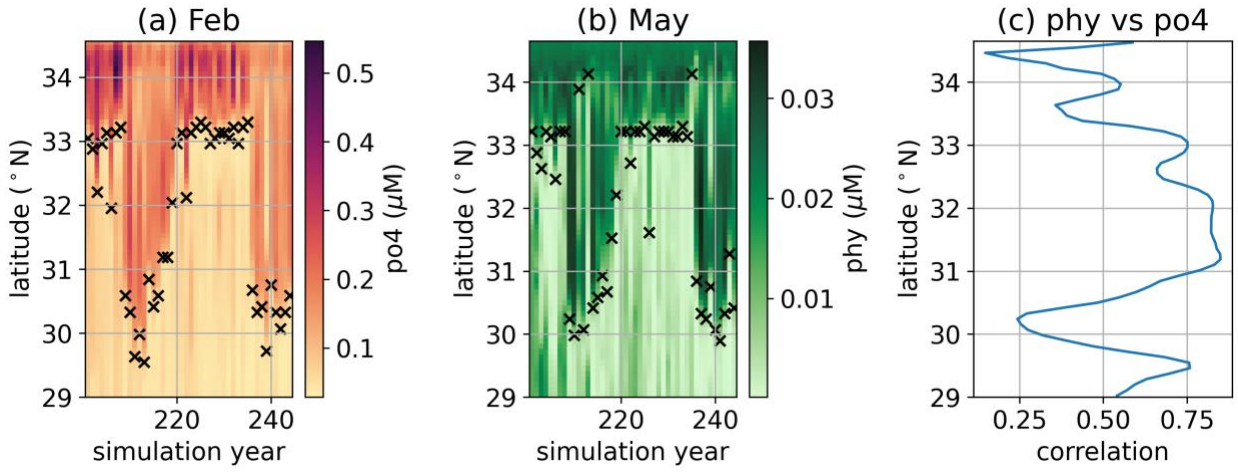

Figure 7. Latitudinal distributions of (a) February surface dissolved phosphate concentration and (b) May surface phytoplankton phosphorous biomass along 137°E over the last 44 years of the model integration. Crosses denote the locations of the Kuroshio axis determined from the sea level gradient along 137°E. (c) Latitudinal distribution of the Pearson's correlation coefficients between the February surface dissolved phosphate concentration and May surface phytoplankton biomass along 137°E over the last 44 years of the model integration.

3.3 Primary Production, Ocean Carbon Uptake, and Export Production

The spatial anomalies of the highs in the offshore region and the lows in the nearshore region during the large meander phase are also present in annual primary production, ocean carbon uptake, and export production (Figure 8). This spatial coherence is expected as higher phytoplankton biomass leads to increased primary production, which results in greater biological carbon uptake and pump. Despite the prominent spatial anomalies, the differences between the

large meander and non-large meander phases are minimal (<5 % difference) when these quantities are integrated over the entire study area.

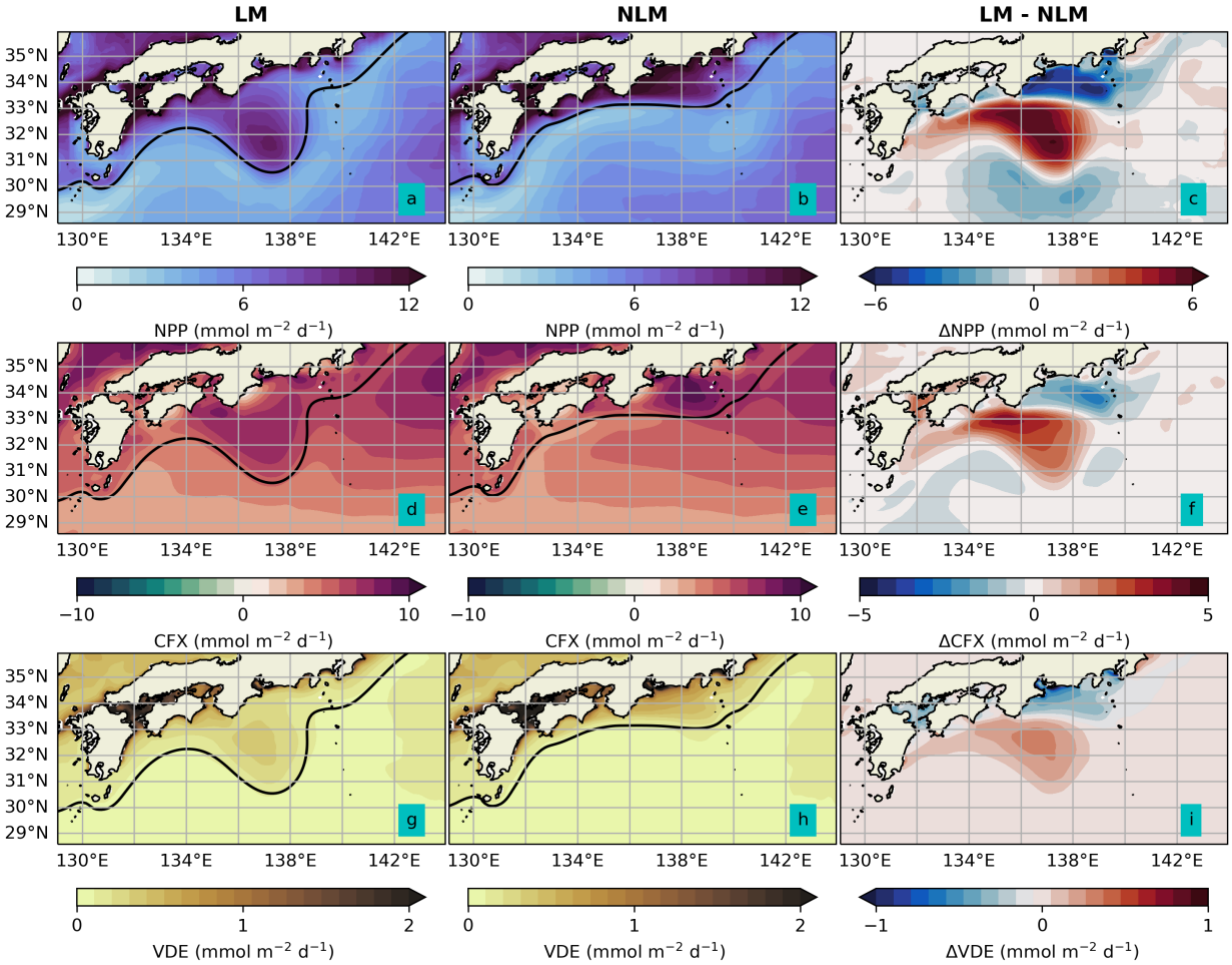

Figure 8. Spatial comparisons of modelled annual mean (a-c) depth-integrated net primary production, (d-f) air-sea carbon flux (positive means flux into the ocean), and (g-i) vertical detritus export at 100 m during the large meanders (a,d,g) and the non-large meanders (b,e,h), and (c,f,i) their differences. Solid lines in (a,b,d,e,g,h) represent the path of the Kuroshio, defined by the annual mean sea level contour at which the latitudinal gradient is maximum along 137°E.

4 Discussion

In this study, we characterized the biogeochemical impacts of the Kuroshio large meander by generating monthly composites of modelled biogeochemical variables during the large meander and non-large meander phases from a multi-decadal simulation output of a 0.1° global sea ice-ocean coupled model. Biogeochemical responses in the model correspond well with the observations even though the Kuroshio axis in the model is generally positioned further south during large meanders. Our spatial analysis reveals that the large meander enhances winter nutrient availability offshore south of Japan by extending the shallow nutricline area that is always positioned on the left side of the Kuroshio path and replenishes the surface water with

nutrients through seasonal convective mixing (Kuroda et al., 2018). The nutrient enrichment in this typically nutrient-poor offshore region during the large meander winter allows phytoplankton to form a bloom a few months later during spring. This offshore large meander bloom arrives a month earlier with a greater magnitude compared to the bloom during the non-large meanders, and is also evident from satellite observations (Lizarbe Barreto et al., 2021). Such a distinct difference in both the timing and magnitude of the spring bloom may alter the spatial distributions of fish abundance and species.

In contrast to the offshore region, the nutrient concentration and phytoplankton biomass in the nearshore region are lower throughout the year during the large meander. This reduction is caused by weakened shoaling effect of the Kuroshio, which makes the subsurface nutrients less accessible by winter convective mixing. The phosphate measurements along 137°N indicate that our model may have overestimated the magnitude of the nutrient reduction during the large meander. On the other hand, the satellite observations suggest that the magnitude of the reduction of the nearshore phytoplankton biomass is similar to that of the offshore increase (Lizarbe Barreto et al., 2021), which is consistent with our model results. In the nearshore region, nutrient availability is important not only for phytoplankton, but also for macroalgae such as seaweed, which is an essential seafood product for Japan.

Essentially, the spatial pattern of the biogeochemical signature of the large meander corresponds to the inverse of temperature anomalies (Sugimoto et al., 2020). However, such biogeochemical anomalies of the large meander will have an influence on macroalgae and higher trophic levels that is disproportionate to the thermal effect. For example, the nearshore warming during the large meander has been related to an increase in sardine egg abundance, whereas the egg abundance of another fish species (anchovy) was more closely linked to water transparency, which is an indicator of food availability (Nakata et al., 2000). Such complexity of fish responses to both physical and biogeochemical processes necessitates more thorough assessment of the large meander impacts on fisheries and aquaculture, which is possible by combining biogeochemical model simulations, satellite ocean color, and in situ monitoring.

Besides the shoaling effect, the Kuroshio path can determine the regional biogeochemical anomalies directly by transporting nutrient-poor waters. It is interesting to note that our model shows a slight decrease in phosphate (Figure 2c) and phytoplankton biomass (Figure 3c) in the Seto Inland Sea during the large meanders. While this result might not be robust because of the limited resolution of the model, previous studies suggested the control of the Kuroshio water intrusion on the hydrographic and biogeochemical properties of the Seto Inland Sea (e.g., Kobayashi & Fujiwara, 2008). Such direct impacts of the Kuroshio remain as a subject of future studies.

A strong correlation between winter nutrient availability and spring phytoplankton bloom in the offshore region gives prospects for improving predictability of the large meander impacts by

implementing biogeochemistry into an operational ocean forecasting system (e.g., Miyazawa et al., 2017). Furthermore, marine industries may benefit from decadal predictions of biogeochemical states, as the decadal variability of the Kuroshio large meander is expected to strengthen in the future due to the stronger decadal variability of the Kuroshio Extension (Joh et al., 2022) that is closely linked to the large meander occurrence (Usui et al., 2013). Such biogeochemical implementation into a decadal ocean prediction system (e.g., Kido et al., 2022) has great potential in supporting long-term adaptation planning for future large meanders that may last longer than the ongoing record-breaking event, as demonstrated by our model simulations.

Appendix

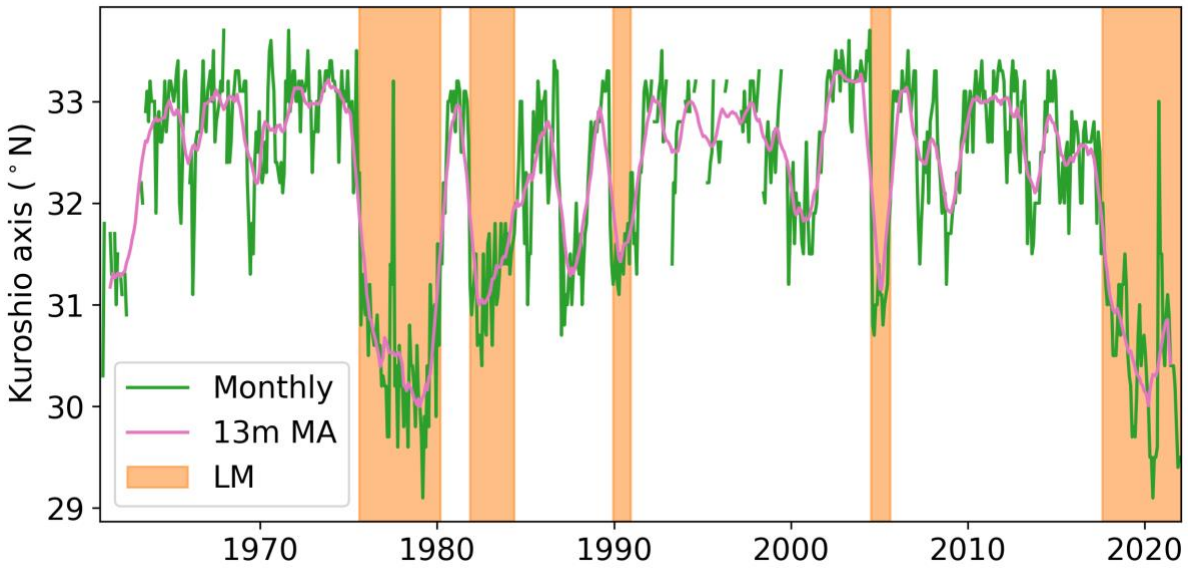

Figure A1. Monthly time series of the Kuroshio axis latitude over 1961-2021 determined by the Japan Meteorological Agency. Green denotes monthly values with the 13-month central moving average indicated by pink. Orange shadings denote the large meander events since 1965.

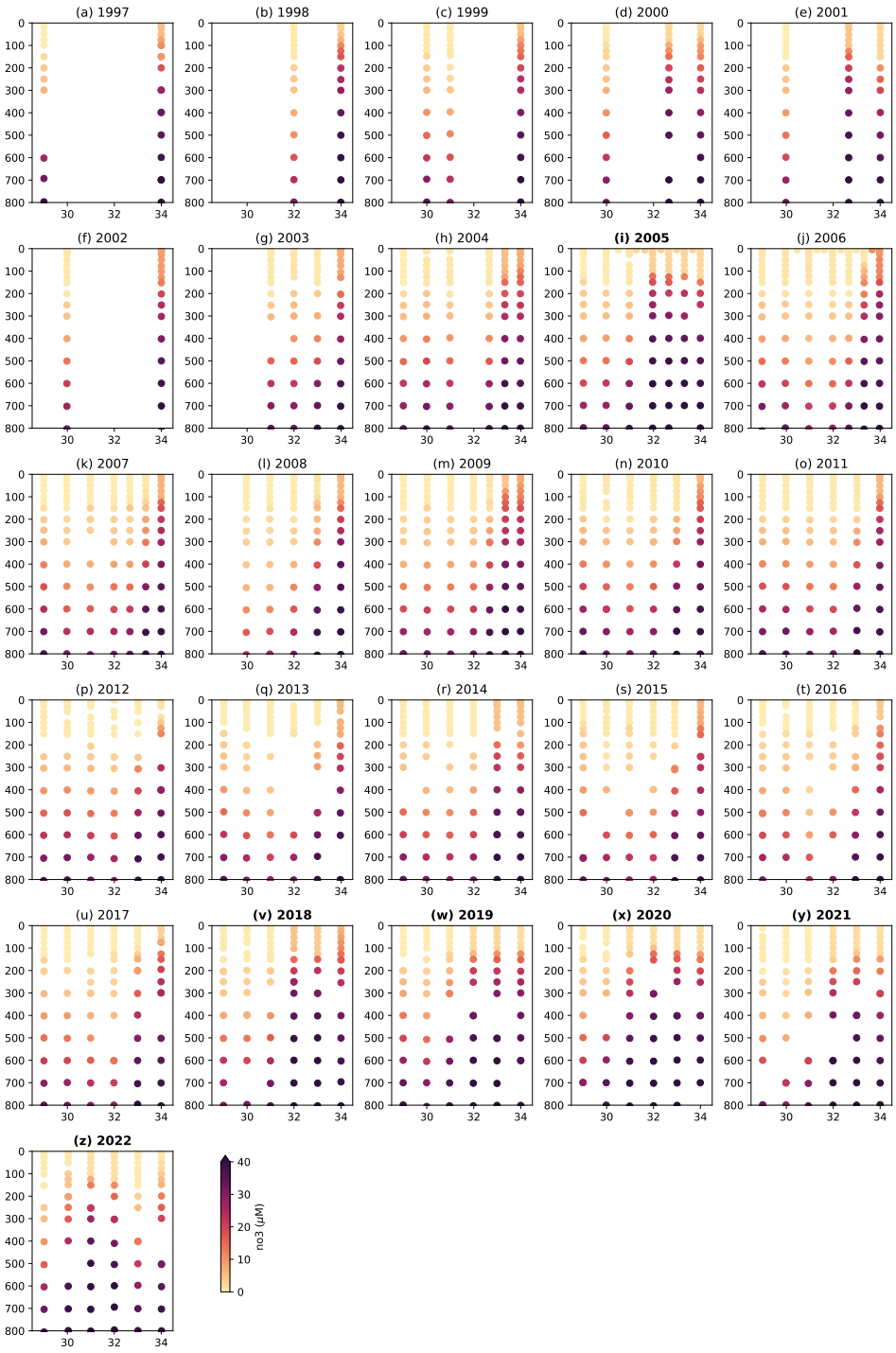

Figure A2. Comparisons of the winter transects of dissolved phosphate concentrations from 29°N to 34°N along 137°E observed annually during late January-early February by the Japan Meteorological Agency since 1997. The large meander years are indicated by bold font in subplot titles.

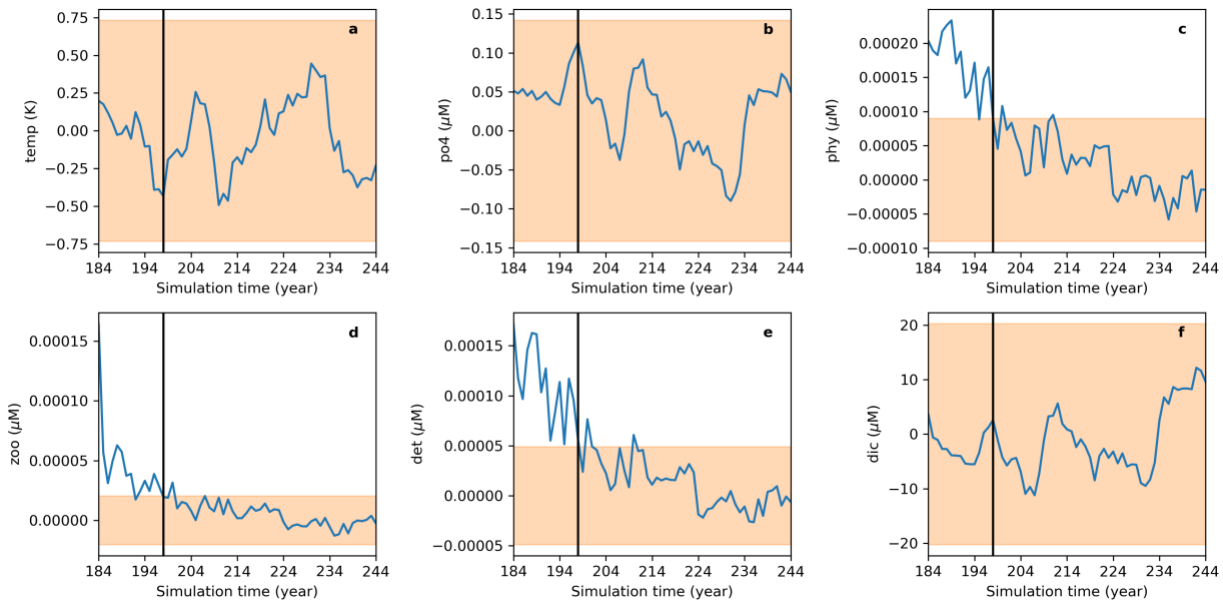

Figure A3. Monthly anomalies of modelled (a) temperature, (b) phosphate concentration, (c) phytoplankton phosphorous biomass, (d) zooplankton phosphorous biomass, (e) detritus phosphorous concentration, and (f) natural dissolved inorganic carbon concentration averaged over the upper 1,000 m of the Kuroshio region (129-144°E by 28-36°N). Values represent anomalies relative to their monthly climatology and shadings denote ±3 standard deviations over the last 30 years of the model integration. Vertical lines denote 15 years after the biogeochemical model initialization.

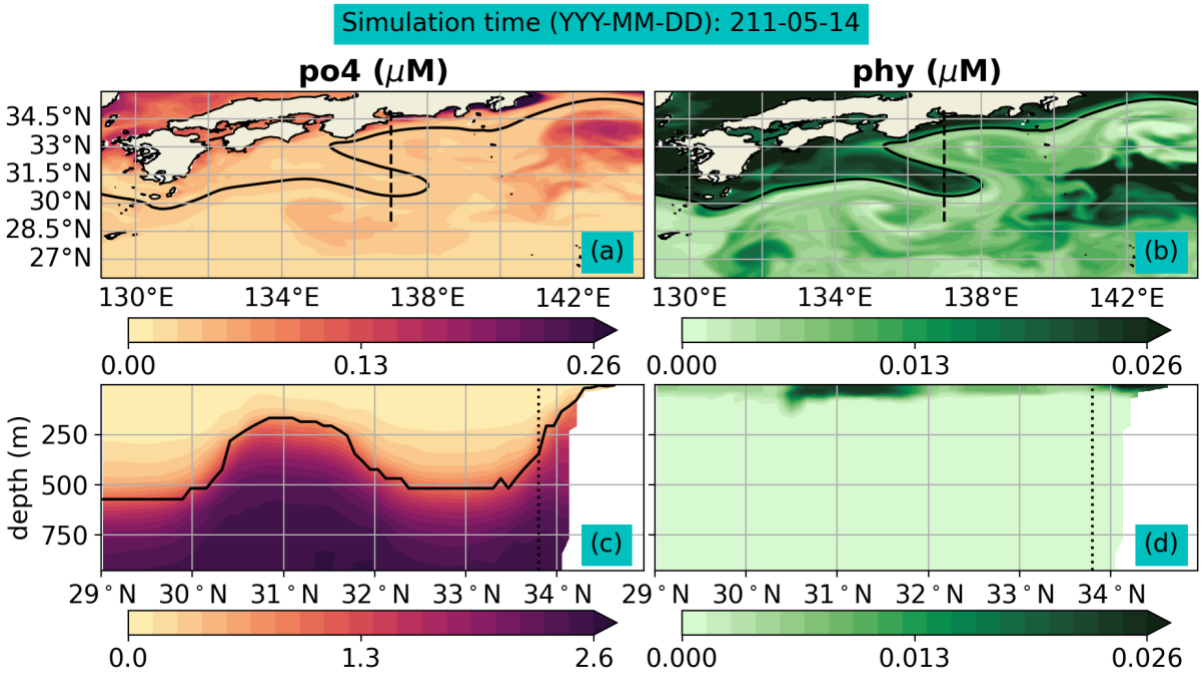

Figure A4. Daily-mean snapshots of modelled (a,c) dissolved phosphate concentration and (b,d)

phytoplankton phosphorous biomass (a,b) in the surface layer and (c,d) along the 137°E latitudinal cross section on May 14 of Year 211. Solid lines in (a) and (b) represent the path of the Kuroshio, defined by the sea level contour at which the latitudinal gradient is maximum along 137°E. Dotted lines in (c) and (d) denote the Kuroshio axis, defined by the latitude at which the latitudinal sea level gradient is maximum along 137°E.

Acknowledgments

Hakase Hayashida and Andrew E. Kiss thank the Consortium for Ocean-Sea Ice Modelling in Australia (COSIMA) team for their support in generating the model output. Andrew E. Kiss was supported by Australian Research Council grants (CE170100023, LP160100073 and LP200100406) and the Australian Government's Australian Antarctic Science Program grant 4541. This project was undertaken with the assistance of resources and services from the National Computational Infrastructure, which is supported by the Australian Government. We thank the Japan Meteorological Agency for making their data publicly available. We do not have conflicts of interest to declare.

Open Research

The ACCESS-OM2-01 output is available to download from http://dx.doi.org/10.25914/608097cb3433f (last accessed on November 28, 2022). The model source code (https://github.com/COSIMA/access-om2; last accessed on November 28, 2022) and configuration (https://github.com/COSIMA/01deg_jra55_iaf/tree/01deg_jra55v140_iaf_cycle4; last accessed on November 28, 2022) are available on github. The hydrographic transect data along 137°E (https://www.data.jma.go.jp/gmd/kaiyou/db/mar_env/results/OI/137E_OI.html#data; last accessed on November 28, 2022) and the monthly Kuroshio axis time series (https://www.data.jma.go.jp/kaiyou/data/shindan/b_2/kuroshio_stream/kuro_slat.txt; last accessed on November 15, 2022) are available to download from the Japan Meteorological Agency website. The observation-based nutrient gridded product is available to download from http://caos.sakura.ne.jp/sao/north-pacific-surface-nutrients/ (last accessed on December 29, 2022).

References

Boyer, T. P., Baranova, O. K., Coleman, C., Garcia, H. E., Grodsky, A., Locarnini, R. A., Mishonov, A. V., Paver, C. R., Reagan, J. R., Seidov, D., Smolyar, I. V., Weathers, K. W., & Zweng, M. M. (2018). *World Ocean Database 2018*. NOAA Atlas NESDIS 87.

Chang, Y.-L. K., Miyazawa, Y., Miller, M. J., & Tsukamoto, K. (2019). Influence of ocean circulation and the Kuroshio large meander on the 2018 Japanese eel recruitment season. *PLOS ONE*, *14*(9), e0223262. https://doi.org/10.1371/journal.pone.0223262

Chang, Y.-L., Miyazawa, Y., Oey, L.-Y., Kodaira, T., & Huang, S. (2017). The formation processes of phytoplankton growth and decline in mesoscale eddies in the western North Pacific Ocean. *Journal of Geophysical Research: Oceans*, *122*(5), 4444–4455. https://doi.org/10.1002/2017JC012722

Griffies, S. M., Danabasoglu, G., Durack, P. J., Adcroft, A. J., Balaji, V., Böning, C. W., Chassignet, E. P., Curchitser, E., Deshayes, J., Drange, H., Fox-Kemper, B., Gleckler, P. J., Gregory, J. M., Haak, H., Hallberg, R. W., Heimbach, P., Hewitt, H. T., Holland, D. M., Ilyina, T., … Yeager, S. G. (2016). OMIP contribution to CMIP6: Experimental and diagnostic protocol for the physical component of the Ocean Model Intercomparison Project. *Geoscientific Model Development*, *9*(9), 3231–3296. https://doi.org/10.5194/gmd-9-3231-2016

Hayashida, H., Matear, R. J., & Strutton, P. G. (2020). Background nutrient concentration determines phytoplankton bloom response to marine heatwaves. *Global Change Biology*, *26*(9), 4800–4811. https://doi.org/10.1111/gcb.15255

Hirata, H., Kawamura, R., Yoshioka, M. K., Nonaka, M., & Tsuboki, K. (2019). Key Role of the Kuroshio Current in the Formation of Frontal Structure of an Extratropical Cyclone Associated with Heavy Precipitation. *Journal of Geophysical Research: Atmospheres*, *124*(12), 6143–6156. https://doi.org/10.1029/2018JD029578

Jeffery, N., Elliott, S. M., Hunke, E. C., Lipscomb, W. H., & Turner, A. K. (2016). *Biogeochemistry of CICE: the Los Alamos Sea Ice Model Documentation and Software User's Manual zbgc_colpkg modifications to Version 5*. https://doi.org/10.2172/1329842

Joh, Y., Delworth, T. L., Wittenberg, A. T., Cooke, W. F., Rosati, A. J., & Zhang, L. (2022). Stronger decadal variability of the Kuroshio Extension under simulated future climate change. *Npj Climate and Atmospheric Science*, *5*(1), Article 1. https://doi.org/10.1038/s41612-022-00285-z

Kasai, A., Kimura, S., & Sugimoto, T. (1993). Warm water intrusion from the Kuroshio into the coastal areas south of Japan. *Journal of Oceanography*, *49*(6), 607–624. https://doi.org/10.1007/BF02276747

Kawabe, M. (1987). Spectral properties of sea level and time scales of Kuroshio path variations. *Journal of the Oceanographical Society of Japan*, *43*(2), 111–123. https://doi.org/10.1007/BF02111887

Kido, S., Nonaka, M., & Miyazawa, Y. (2022). JCOPE-FGO: An eddy-resolving quasi-global ocean reanalysis product. *Ocean Dynamics*. https://doi.org/10.1007/s10236-022-01521-z

Kiss, A. E., Hogg, A. M., Hannah, N., Boeira Dias, F., Brassington, G. B., Chamberlain, M. A., Chapman, C., Dobrohotoff, P., Domingues, C. M., Duran, E. R., England, M. H., Fiedler, R., Griffies, S. M., Heerdegen, A., Heil, P., Holmes, R. M., Klocker, A., Marsland, S. J., Morrison, A. K., … Zhang, X. (2020). ACCESS-OM2 v1.0: A global ocean–sea ice model at three resolutions. *Geoscientific Model Development*, *13*(2), 401–442. https://doi.org/10.5194/gmd-13-401-2020

Kobayashi, S., & Fujiwara, T. (2008). Long-term variability of shelf water intrusion and its influence on hydrographic and biogeochemical properties of the Seto Inland Sea, Japan. *Journal of Oceanography*, *64*(4), 595–603. https://doi.org/10.1007/s10872-008-0050-0

Kuroda, H., Takasuka, A., Hirota, Y., Kodama, T., Ichikawa, T., Takahashi, D., Aoki, K., & Setou, T. (2018). Numerical experiments based on a coupled physical–biochemical ocean model to study the Kuroshio-induced nutrient supply on the shelf-slope region off the southwestern coast of Japan. *Journal of Marine Systems*, *179*, 38–54. https://doi.org/10.1016/j.jmarsys.2017.11.002

Lauvset, S. K., Key, R. M., Olsen, A., van Heuven, S., Velo, A., Lin, X., Schirnick, C., Kozyr, A., Tanhua, T., Hoppema, M., Jutterström, S., Steinfeldt, R., Jeansson, E., Ishii, M., Perez, F. F., Suzuki, T., & Watelet, S. (2016). A new global interior ocean mapped climatology: The 1-deg. by 1-deg. GLODAP version 2. *Earth System Science Data*, *8*, 325–340. https://doi.org/10.5194/essd-8-325-2016

Lauvset, S. K., Lange, N., Tanhua, T., Bittig, H. C., Olsen, A., Kozyr, A., Alin, S. R., Álvarez, M., Azetsu-Scott, K., Barbero, L., Becker, S., Brown, P. J., Carter, B. R., da Cunha, L. C., Feely, R. A., Hoppema, M., Humphreys, M. P., Ishii, M., Jeansson, E., … Key, R. M. (2022). GLODAPv2.2022: The latest version of the global interior ocean biogeochemical data product. *Earth System Science Data Discussions*, 1–37. https://doi.org/10.5194/essd-2022-293

Lizarbe Barreto, D. A., Chevarria Saravia, R., Nagai, T., & Hirata, T. (2021). Phytoplankton Increase Along the Kuroshio Due to the Large Meander. *Frontiers in Marine Science*, *8*. https://www.frontiersin.org/articles/10.3389/fmars.2021.677632

Long, Y., Zhu, X.-H., Guo, X., & Huang, H. (2018). Temporal Variation of Kuroshio Nutrient Stream South of Japan. *Journal of Geophysical Research: Oceans*, *123*(11), 7896–7913. https://doi.org/10.1029/2017JC013635

Mackallah, C., Chamberlain, M. A., Law, R. M., Dix, M., Ziehn, T., Bi, D., Bodman, R., Brown, J. R., Dobrohotoff, P., Druken, K., Evans, B., Harman, I. N., Hayashida, H., Holmes, R., Kiss, A. E., Lenton, A., Liu, Y., Marsland, S., Meissner, K., … Yeung, N. (2022). ACCESS datasets for CMIP6: Methodology and idealised experiments. *Journal of Southern Hemisphere Earth Systems Science*, *72*(2), 93–116. https://doi.org/10.1071/ES21031

Miyama, T., & Miyazawa, Y. (2013). Structure and dynamics of the sudden acceleration of Kuroshio off Cape Shionomisaki. *Ocean Dynamics*, *63*(2), 265–281. https://doi.org/10.1007/s10236-013-0591-7

Miyazawa, Y., Varlamov, S. M., Miyama, T., Guo, X., Hihara, T., Kiyomatsu, K., Kachi, M., Kurihara, Y., & Murakami, H. (2017). Assimilation of high-resolution sea surface temperature data into an operational nowcast/forecast system around Japan using a multi-scale three-dimensional variational scheme. *Ocean Dynamics*, *67*(6), 713–728. https://doi.org/10.1007/s10236-017-1056-1

Moore, C. M., Mills, M. M., Arrigo, K. R., Berman-Frank, I., Bopp, L., Boyd, P. W., Galbraith, E. D., Geider, R. J., Guieu, C., Jaccard, S. L., Jickells, T. D., La Roche, J., Lenton, T. M., Mahowald, N. M., Marañón, E., Marinov, I., Moore, J. K., Nakatsuka, T., Oschlies, A., … Ulloa, O. (2013). Processes and patterns of oceanic nutrient limitation. *Nature Geoscience*, *6*(9), Article 9. https://doi.org/10.1038/ngeo1765

582 Nakata, H., Funakoshi, S., & Nakamura, M. (2000). Alternating dominance of postlarval sardine
583 and anchovy caught by coastal fishery in relation to the Kuroshio meander in the Enshu-
584 nada Sea. *Fisheries Oceanography*, *9*(3), 248–258. https://doi.org/10.1046/j.1365-
585 2419.2000.00140.x
586 Oka, E., Ishii, M., Nakano, T., Suga, T., Kouketsu, S., Miyamoto, M., Nakano, H., Qiu, B.,
587 Sugimoto, S., & Takatani, Y. (2018). Fifty years of the 137°E repeat hydrographic
588 section in the western North Pacific Ocean. *Journal of Oceanography*, *74*(2), 115–145.
589 https://doi.org/10.1007/s10872-017-0461-x
590 Oke, P. R., Griffin, D. A., Schiller, A., Matear, R. J., Fiedler, R., Mansbridge, J., Lenton, A.,
591 Cahill, M., Chamberlain, M. A., & Ridgway, K. (2013). Evaluation of a near-global
592 eddy-resolving ocean model. *Geoscientific Model Development*, *6*(3), 591–615.
593 https://doi.org/10.5194/gmd-6-591-2013
594 Orr, J. C., Najjar, R. G., Aumont, O., Bopp, L., Bullister, J. L., Danabasoglu, G., Doney, S. C.,
595 Dunne, J. P., Dutay, J.-C., Graven, H., Griffies, S. M., John, J. G., Joos, F., Levin, I.,
596 Lindsay, K., Matear, R. J., McKinley, G. A., Mouchet, A., Oschlies, A., … Yool, A.
597 (2017). Biogeochemical protocols and diagnostics for the CMIP6 Ocean Model
598 Intercomparison Project (OMIP). *Geoscientific Model Development*, *10*(6), 2169–2199.
599 https://doi.org/10.5194/gmd-10-2169-2017
600 Qiu, B., & Chen, S. (2021). Revisit of the Occurrence of the Kuroshio Large Meander South of
601 Japan. *Journal of Physical Oceanography*, *51*(12), 3679–3694.
602 https://doi.org/10.1175/JPO-D-21-0167.1

Qiu, B., & Miao, W. (2000). Kuroshio Path Variations South of Japan: Bimodality as a Self-Sustained Internal Oscillation. *Journal of Physical Oceanography*, *30*(8), 2124–2137. https://doi.org/10.1175/1520-0485(2000)030<2124:KPVSOJ>2.0.CO;2

Sakajo, T., Ohishi, S., & Uda, T. (2022). Identification of Kuroshio meanderings south of Japan via a topological data analysis for sea surface height. *Journal of Oceanography*, *78*(6), 495–513. https://doi.org/10.1007/s10872-022-00656-3

Sugimoto, S., Qiu, B., & Kojima, A. (2020). Marked coastal warming off Tokai attributable to Kuroshio large meander. *Journal of Oceanography*, *76*(2), 141–154. https://doi.org/10.1007/s10872-019-00531-8

Sugimoto, S., Qiu, B., & Schneider, N. (2021). Local Atmospheric Response to the Kuroshio Large Meander Path in Summer and Its Remote Influence on the Climate of Japan. *Journal of Climate*, *34*(9), 3571–3589. https://doi.org/10.1175/JCLI-D-20-0387.1

Tagliabue, A., Aumont, O., DeAth, R., Dunne, J. P., Dutkiewicz, S., Galbraith, E., Misumi, K., Moore, J. K., Ridgwell, A., Sherman, E., Stock, C., Vichi, M., Völker, C., & Yool, A. (2016). How well do global ocean biogeochemistry models simulate dissolved iron distributions? *Global Biogeochemical Cycles*, *30*(2), 149–174. https://doi.org/10.1002/2015GB005289

Tochimoto, E., & Iizuka, S. (2022). Impact of warm sea surface temperature over a Kuroshio large meander on extreme heavy rainfall caused by an extratropical cyclone. *Atmospheric Science Letters*, *n/a*(n/a), e1135. https://doi.org/10.1002/asl.1135

Tsujino, H., Nishikawa, S., Sakamoto, K., Usui, N., Nakano, H., & Yamanaka, G. (2013). Effects of large-scale wind on the Kuroshio path south of Japan in a 60-year historical

OGCM simulation. *Climate Dynamics*, *41*(9), 2287–2318. https://doi.org/10.1007/s00382-012-1641-4

Tsujino, H., Urakawa, L. S., Griffies, S. M., Danabasoglu, G., Adcroft, A. J., Amaral, A. E., Arsouze, T., Bentsen, M., Bernardello, R., Böning, C. W., Bozec, A., Chassignet, E. P., Danilov, S., Dussin, R., Exarchou, E., Fogli, P. G., Fox-Kemper, B., Guo, C., Ilicak, M., … Yu, Z. (2020). Evaluation of global ocean–sea-ice model simulations based on the experimental protocols of the Ocean Model Intercomparison Project phase 2 (OMIP-2). *Geoscientific Model Development*, *13*(8), 3643–3708. https://doi.org/10.5194/gmd-13-3643-2020

Tsujino, H., Urakawa, S., Nakano, H., Small, R. J., Kim, W. M., Yeager, S. G., Danabasoglu, G., Suzuki, T., Bamber, J. L., Bentsen, M., Böning, C. W., Bozec, A., Chassignet, E. P., Curchitser, E., Boeira Dias, F., Durack, P. J., Griffies, S. M., Harada, Y., Ilicak, M., … Yamazaki, D. (2018). JRA-55 based surface dataset for driving ocean–sea-ice models (JRA55-do). *Ocean Modelling*, *130*, 79–139. https://doi.org/10.1016/j.ocemod.2018.07.002

Usui, N., Tsujino, H., Nakano, H., & Matsumoto, S. (2013). Long-term variability of the Kuroshio path south of Japan. *Journal of Oceanography*, *69*(6), 647–670. https://doi.org/10.1007/s10872-013-0197-1

Virtanen, P., Gommers, R., Oliphant, T. E., Haberland, M., Reddy, T., Cournapeau, D., Burovski, E., Peterson, P., Weckesser, W., Bright, J., van der Walt, S. J., Brett, M., Wilson, J., Millman, K. J., Mayorov, N., Nelson, A. R. J., Jones, E., Kern, R., Larson, E., … van Mulbregt, P. (2020). SciPy 1.0: Fundamental algorithms for scientific computing in Python. *Nature Methods*, *17*(3), Article 3. https://doi.org/10.1038/s41592-019-0686-2

Yasunaka, S., Mitsudera, H., Whitney, F., & Nakaoka, S. (2021). Nutrient and dissolved inorganic carbon variability in the North Pacific. *Journal of Oceanography*, *77*(1), 3–16. https://doi.org/10.1007/s10872-020-00561-7

Yoneda, M., Fujita, T., Yamamoto, M., Tadokoro, K., Okazaki, Y., Nakamura, M., Takahashi, M., Kono, N., Matsubara, T., Abo, K., Xinyu, G., & Yoshie, N. (2022). Bottom-up processes drive reproductive success of Japanese anchovy in an oligotrophic sea: A case study in the central Seto Inland Sea, Japan. *Progress in Oceanography*, *206*, 102860. https://doi.org/10.1016/j.pocean.2022.102860

Zhu, Y., Minami, K., Iwahara, Y., Oda, K., Hidaka, K., Hoson, O., Morishita, K., Hirota, M., Tsuru, S., Shirakawa, H., & Miyashita, K. (2021). Seasonal variation in fish school spatial distribution and abundance under the Kuroshio regular pattern and the large meander in Suzu coastal waters. *PLOS ONE*, *16*(11), e0260629. https://doi.org/10.1371/journal.pone.0260629

Ziehn, T., Chamberlain, M. A., Law, R. M., Lenton, A., Bodman, R. W., Dix, M., Stevens, L., Wang, Y.-P., Srbinovsky, J., Ziehn, T., Chamberlain, M. A., Law, R. M., Lenton, A., Bodman, R. W., Dix, M., Stevens, L., Wang, Y.-P., & Srbinovsky, J. (2020). The Australian Earth System Model: ACCESS-ESM1.5. *Journal of Southern Hemisphere Earth Systems Science*, *70*(1), 193–214. https://doi.org/10.1071/ES19035